

IMPLEMENTATION OF THE FINITE-DIFFERENCE TIME-DOMAIN
METHOD USING GRAPHICS PROCESSING UNITS

Approved by:

Dr. Marc Christensen

Dr. Nathan Huntoon

Professor Ira Greenberg

IMPLEMENTATION OF THE FINITE-DIFFERENCE TIME-DOMAIN
METHOD USING GRAPHICS PROCESSING UNITS

A Thesis Presented to the Graduate Faculty of the
Lyle School of Engineering
Southern Methodist University

in

Partial Fulfillment of the Requirements

for the degree of

Master of Electrical Engineering

with a

Major in Electrical Engineering

by

S. David Lively

(B.S.E.E, Southern Methodist University, 2008)

August 1, 2016

ACKNOWLEDGMENTS

I thank my committee for their patience, insight and unfailing encouragement. Without them, this thesis would remain vaporware. Never give up, never surrender!

Lively , S. David

B.S.E.E, Southern Methodist University, 2008

Implementation of the Finite-Difference Time-Domain
Method Using Graphics Processing Units

Advisor: Professor Marc Christensen
Master of Electrical Engineering degree conferred August 1, 2016
Thesis completed

Traditionally, optical circuit design is tested and validated using software which implement numerical modeling techniques such as Beam Propagation, Finite Element Analysis and FDTD.

While effective and accurate, FDTD simulations require significant computational power. Existing installations may distribute the computational requirements across large clusters of high-powered servers. This approach entails significant expense in terms of hardware, staffing and software support which may be prohibitive for some research facilities and private-sector engineering firms.

Application of modern programmable GPGPUs to problems in scientific visualization and computation has facilitated dramatically accelerated development cycles for a variety of industry segments including large dataset visualization, microprocessor design, aerospace and electromagnetic wave propagation in the context of optical circuit design. The FDTD algorithm as envisioned by its creators maps well to the massively-multithreaded data-parallel nature of GPUs. This thesis explores a GPU FDTD implementation and details performance gains, limitations of the GPU approach, optimization techniques and potential future enhancements that may provide even greater benefits from this underutilized and often-overlooked tool.

TABLE OF CONTENTS

LIST OF FIGURES	v
LIST OF TABLES	vi
CHAPTER	
1. INTRODUCTION	1
1.1. Homogeneous Isotropic Turbulence	2
1.2. Moments of the Inertial Range.....	4
1.2.1. Mellin Transforms.....	4
1.3. Scaling Exponents.....	6
1.4. Methods for Obtaining Data from the Inertial Range.....	8
1.5. Organization of the Chapters	8
2. APPLYING THE NEW SIMILARITY THEORY TO THE SHELL MODEL DATA	10
2.1. Determination of n_0 and C_3 via Rescaled Structure Functions	11
2.1.1. The Limit of $p \rightarrow 0$	13
2.2. Graphically Measured Collapse	16
APPENDIX	
A. APPENDIX.....	20
A.1. Description of GOY Shell Model Runs and Table.....	20
A.2. Description of Sabra Shell Model Runs and Table	22
REFERENCES	24

LIST OF FIGURES

Figure	Page
1.1. Sketch of an energy spectrum. (eps file)	3
2.1. Rescaled structure function of Run 9 from Table A.2 (Sabra). The functions can be formed because we have found universal coefficients. $p = [-1.75, -1.5, \dots, -0.5, -0.25, 0, 0.5, 1.0, \dots, 11.5, 12.0]$..	14
2.2. Rescaled structure function of Run 9 from Table A.2 (a) with $p = 0$ included. Note the gap between the negative and positive p values. (b) as $p \rightarrow 0$ where $0.1 \geq p \geq 0.01$. Clearly a limit exists. ...	15
2.3. Individual plots of each of the radial profiles that have a similar curve. The radial profiles $P_0(r; n)$ plotted on log-log scales for $3 \leq n \leq 20$ for Sabra Run 9.	19
A.1. Distribution of u_i . This plot displays the quasi-periodic nature of Run 3 for shell 10 (eps file).	21

LIST OF TABLES

Table	Page
2.1. Measurements for scaling individual radial profiles. Shell 12 is selected as the radial profile to be scaled to. The fixed scale refers to the Shell 12 axis. The first pair of fixed and stretched scales refers to the initial alignment of the horizontal axis. The second pair refers to the terminal alignment of the horizontal axis.	18
A.1. Simulations with the GOY shell model with respective parameters. Run 1 uses the original GOY form found in (??). Runs 2-10 use the log polar form of GOY found in (??).	22
A.2. Simulations with the Sabra shell model with respective parameters. Run 1 uses the original Sabra form found in (??). Runs 2-10 use the log polar form of Sabra found in (??).	23

*Dedicated to my amazing wife and best friend, Audrey, and our children Wyatt,
Walter and Gwendolyn.*

Chapter 1

INTRODUCTION

The construction of optical circuits and systems is a complex and expensive process. Engineers invest substantial resources in the design and fabrication of a circuit. Given the scale and expense involved in realizing even the simplest system, it is necessary to model or simulate circuits before fabrication in order to validate designs and ensure that they meet project requirements.

While many simulation techniques exist, this paper focuses on the finite-difference, time-domain (FDTD) method and its implementation.

Although conceptually simple, FDTD in large scale requires significant computational resources in order to facilitate a quick, iterative design process. One way to address this challenge is employ clusters of powerful computers. By distributing a simulation across a cluster, capabilities may be scaled in two ways. The increased memory makes it possible to solve larger problems which may not fit within the relatively limited resources available on a single machine. Increased processing power reduces the amount of time that is required to solve a given problem.

While effective, this approach presents several challenges. Provisioning of clusters of powerful computers is an expensive proposition, and may strain or exceed the budgets of smaller organizations. Even within institutions which possess the required compute resources, high demand for access to said resources may present a bottleneck, again slowing the iterative design process which this approach was intended to solve.

Another approach, which has not gained adoption among FDTD software providers, is the use of graphics processing units (GPUs) to solve highly parallelizable problems.

While a relatively new field of study, the applicationn of GPUs to general computing problems as promising, and has already yielded impressive results in areas such as medical research, machine learning, artificial intelligence and others.

This paper explores a GPU-based implementation of FDTD and examines it's performance relative to existing CPU-based implementations.

1.1. Homogeneous Isotropic Turbulence

The governing equations are the incompressible Navier Stokes equations:

$$\frac{\partial \mathbf{u}}{\partial t} + (\mathbf{u} \cdot \nabla) \mathbf{u} = -\frac{1}{\rho} \nabla p + \nu \nabla^2 \mathbf{u} + \mathbf{F}, \quad (1.1)$$

$$\nabla \cdot \mathbf{u} = 0, \quad (1.2)$$

where \mathbf{u} is the flow velocity, ρ is the fluid density, p is the pressure, ν is the kinematic viscosity, and \mathbf{F} is the forcing. The density is constant so there are no buoyancy effects. The viscosity is also constant. Moreover, the fluid is unbounded so there are no walls and boundary layers. We consider an idealized forcing specified in wave number space at a single spatial frequency so that we have homogeneity and isotropy. Under these circumstances we can transform the entire problem to Fourier space. There, a single equation describes the problem:

$$\left(\frac{\partial}{\partial t} + \nu k^2 \right) \hat{u}_i(\vec{k}, t) = -ik_m P_{ij}(\vec{k}) \int_{\vec{p}+\vec{q}=\vec{k}} \hat{u}_j(\vec{p}, t) \hat{u}_m(\vec{q}, t) d\vec{p} + \hat{F}_i(\vec{k}), \quad (1.3)$$

where \hat{u} is the Fourier transform of u , \hat{u}_i is the i -component of the Fourier velocity vector, k is the wave number, \hat{F} is the Fourier transform of the forcing, \vec{k} , \vec{p} and \vec{q} are wave vectors

$$P_{ij}(\vec{k}) = \delta_{i,j} - \frac{k_i k_j}{k^2} \quad (1.4)$$

is the projection operator that removes the pressure term. This is the traditional starting point for the study of homogeneous isotropic turbulence [3, 10, 13] which

always develops when the forcing is strong enough to give a high Reynolds number.

Homogeneity and isotropy refers to independence of location and orientation in space. The first to utilize this type of turbulence was G.I. Taylor [23]. With these properties it makes sense to talk about energy per unit volume, e.g.

$$E = \frac{1}{2} \langle |\vec{u}|^2 \rangle_{\text{unit box}}. \quad (1.5)$$

where $\langle \rangle$ means average and unit box is defined as $[0, 1]$ by $[0, 1]$ by $[0, 1]$. It is traditional to decompose the energy according to the wave number in Fourier space. This gives the energy spectrum $E(|\vec{k}|)$ which is typically plotted on double logarithmic scales as sketched in Figure 1.1. The reason for using the double logarithmic scales

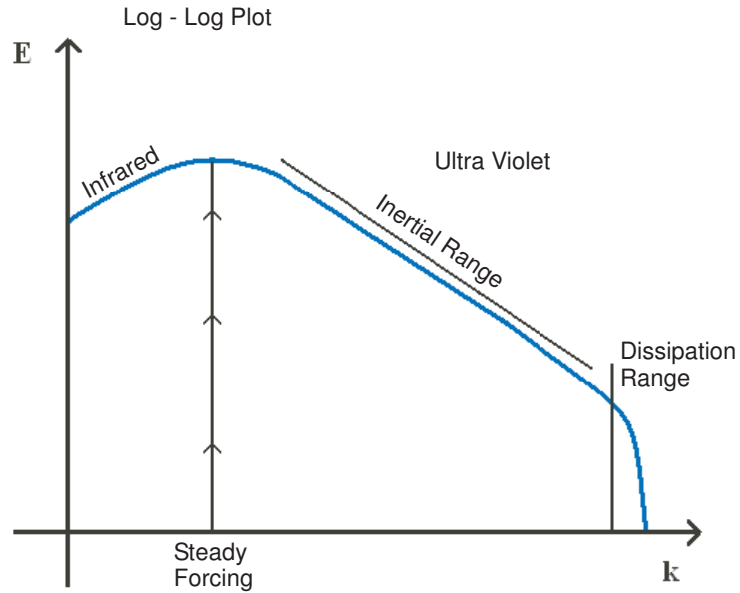


Figure 1.1. Sketch of an energy spectrum. (eps file)

is that some parts of the spectrum obey power laws and thus become straight lines in Figure 1.1. In particular, the inertial range obeys a power law with slope $-5/3$

or nearly so. The $-5/3$ value was obtained theoretically by Kolmogorov 1941 via a scaling argument together with his four-fifth's law [11]. Experimental evidence [7, 9, 4] has confirmed an inertial range with slope near $-5/3$.

1.2. Moments of the Inertial Range

To study the inertial range, moments of various quantities are employed. The energy spectrum is just one example of an inertial range moment obeying a power law; other examples include $\langle |\hat{u}(\vec{k})|^p \rangle$. There is a transform specifically designed to deal with moments, namely, the Mellin transform. It is related to the more familiar Fourier and Laplace transform through various manipulations in the complex plane; see [22].

1.2.1. Mellin Transforms

The Mellin transform is defined as

$$\Phi(z) = \mathcal{M}[\phi(x); z] \equiv \int_0^\infty x^{z-1} \phi(x) dx. \quad (1.6)$$

When $\phi(x)$ is a probability density function of a *positive* random variable X ,

$$\phi(x)dx = Pr\{x < X < x + dx\}, \quad x > 0, \quad (1.7)$$

then the moments of X are

$$\langle X^p \rangle = \int_0^\infty x^p \phi(x) dx. \quad (1.8)$$

Next, we introduce x into the equation so that we may write moments in terms of Mellin transforms;

$$\begin{aligned} &= \int_0^\infty x^{p+1} \phi(x) \frac{dx}{x} \\ &= \mathcal{M}[\phi(x); p+1]. \end{aligned} \quad (1.9)$$

Since the random variable is positive, moments of non-integer orders are readily defined¹. The only restriction on p is that the improper integral must converge. The function ϕ is then uniquely determined from its moments through the inverse Mellin transform. It, like the inverse Laplace transform, involves a contour integral in the complex plane.

In order to use the Mellin transform in our investigations, it is necessary that we know how various self-similarities transform. Suppose, our pdf, ϕ , depends parametrically on a length scale, ℓ , i.e. $\phi = \phi(x, \ell)$, in a self-similar way where $\ell = 2\pi/k$. For example, we could have

$$\phi(x, \ell) = C(\ell) f\left(\frac{x}{\sigma(\ell)}\right), \quad (1.10)$$

where $\sigma = \langle X^2 \rangle^{1/2}$ and $f(x) \geq 0$, represents the similarity profile. Of course, C would then be specified by the requirement that $\phi(x, \ell)$ be a pdf, i.e.

$$\int_0^\infty \phi(x, \ell) dx = C \int_0^\infty f\left(\frac{x}{\sigma(\ell)}\right) dx = 1 \quad (1.11)$$

$$\Rightarrow C = \left(\sigma \int_0^\infty f(u) du\right)^{-1} = \sigma^{-1}. \quad (1.12)$$

For the Mellin transform, we then have

$$\begin{aligned} \mathcal{M}[\phi(x; \ell); z] &= C \mathcal{M}\left[f\left(\frac{x}{\sigma}\right); z\right] \\ &= C \sigma^z \mathcal{M}[f(x); z] \\ &= \sigma^{z-1} \frac{F(z)}{F(1)} \end{aligned} \quad (1.13)$$

where $F(z) = \mathcal{M}[f(x); z]$ and $F(1) = 1$ only if $f(x)$ is a pdf.

¹We can also use Mellin transforms for a random variable that is only real rather than positive. To do this, we split ϕ unto its odd and even parts. Each part can then be treated similarly to (1.9).

Correspondingly, we have

$$\langle X^p \rangle = \mathcal{M}[\phi(x; \ell); p+1] = \frac{\sigma^p(\ell) F(p+1)}{F(1)} \quad (1.14)$$

and

$$\langle X \rangle^p = \mathcal{M}[\phi(x; \ell); 2]^p = \left(\frac{\sigma(\ell) F(2)}{F(1)} \right)^p, \quad (1.15)$$

so that the dimensionless ratio

$$\frac{\langle X^p \rangle}{\langle X \rangle^p} = \frac{F(p+1)}{F(1)} \left(\frac{F(2)}{F(1)} \right)^p \quad (1.16)$$

is independent of ℓ . The self-similarity (1.10), also known as global scaling invariance or statistical self-similarity, was used by Kolmogorov as a postulate in his 1941 theory to obtain the $-5/3$ slope [11]. From (1.16) it follows that the corresponding exponents are linear, i.e. if $\langle X^p \rangle = C_p \ell^{\zeta_p}$ then $\zeta_p = p\zeta_1$.

1.3. Scaling Exponents

In the inertial range, the moments of almost any numerical value one can think of are power laws in the scale. When working in Fourier space the magnitude of the wave number $|\vec{k}|$ defines the scale. However, not all theoretical investigations use Fourier space. The Karmon-Howarth equation [10], for example, works with a spatial length scale. This equation, formulated in the thirties, uses two point spatial correlations for the reason that these are readily obtained experimentally. Specifically, velocity differences between two points depend only on the separation distance ℓ when the turbulence is homogeneous and isotropic. Only two velocity differences come into play: $\delta v_{\parallel}(\ell)$ and $\delta v_{\perp}(\ell)$. The former is parallel to the line segment connecting the two points, the latter perpendicular to it. For the second order moments, e.g. $\langle (\delta v_{\parallel})^2 \rangle$, a direct connection can be established with Fourier space through Parseval's identity. For other orders there is, unfortunately, no similar connection.

The four-fifth's law of Kolmogorov in 1941 was formulated in terms of $\delta v_{\parallel}(\ell)$. This states

$$\langle (\delta v_{\parallel})^3 \rangle = -\frac{4}{5}\epsilon\ell \quad (1.17)$$

where ϵ is the dissipation. Combining the four-fifth's-law with the assumption of statistical self-similarity (1.10), he readily obtained

$$\langle (\delta v_{\parallel})^p \rangle = C_p \ell^{\zeta_p} = \tilde{C}_p \epsilon^{p/3} \ell^{p/3} \quad (1.18)$$

with $\zeta_p = \zeta_3 p/3 = p/3$, where C_p are supposedly universal coefficients. This scaling law is commonly called K41. Note ζ_p is a linear function of p . The -5/3 slope of the energy spectrum is a direct consequence of K41. The idea of universal coefficients soon was questioned by Landau [7]. Since the sixties it also has become clear that the scaling exponents ζ_p are nonlinear, which is referred to as anomalous scaling and is often associated with intermittent fluctuations.

Experimental evidence [2, 18, 20, 24] conclusively shows that ζ_p is nonlinear, but also show that the four-fifth's law is valid. There have been many attempts at modeling the anomalous scaling. Kolmogorov in 1962 suggested that ζ_p should be quadratic in his log normal theory. By using a matched asymptotic expansion Lundgren has produced a model in which K41 and anomalous scaling results are present [12]. The moments are given as an integral that depends on a function $f(q)$, where $f(q)$ has a peak close to $q = 1/3$. If $q = 1/3$, then K41 is produced. However, if $q < 1/3$, then anomalous scaling is produced [12]. Another model that mimics observed scaling exponents is the Log-Poisson model of She and Leveque [21]. They argue that the moment ratios create a universal relationship between consecutive structures. This in turn led to the scaling exponents we use in Chapter ???. The data that came from the experiment done by [2] was the foundation for another model. After observing their data, Parisi and Frisch decided to weaken the global scale-invariance of K41 and use a local scale-invariance [1]. Each of these models produces anomalous scaling.

1.4. Methods for Obtaining Data from the Inertial Range

In order to study the inertial range, we need to obtain numerical data. There are at least three different approaches one can take: physical experiments [25]; direct numerical simulations of the Navier Stokes equations [17]; and numerical studies of models of the Navier Stokes equations [7]. There are advantages and shortcomings to each approach. In the physical experiment all the effects of Navier Stokes equations are, of course, present in real form. However, homogeneous and isotropic turbulence is an idealization which can only be approximated in an experimental facility. Moreover, the data may not be obtainable in the form one would like. In particular, experiments usually provide time series of velocity increments δv_{\parallel} and δv_{\perp} for various separations whereas one would like to know the Fourier decomposition of the velocity.

Direct numerical simulations of the Navier Stokes equations do provide the Fourier decomposition but at limited Reynolds numbers. It is difficult to have high resolution in the entire inertial range and still have an adequate dissipation range. The periodic box effect, inherent in the usual spectral codes, is also a problem at the larger scales. In spite of these shortcomings, direct numerical simulations are undoubtedly the best at providing data. The computational resources are, however, well outside the range of what is reasonable for this thesis.

For this reason, we resort to studying models of Navier Stokes equations in wave number space. Such models are known as shell models and allow us to consider very high Reynolds numbers. In fact, the limit of infinite Reynolds numbers is approachable. Moreover, the computational resource requirements are modest.

1.5. Organization of the Chapters

In Chapter ?? will we explore the use of stretched exponentials as functions to describe inertial range pdf's. However, we find that this class of functions fail because

they do not admit for power law scaling in the inertial range. Chapter ?? investigates pdf's constructed from given scaling exponents. In particular, we look at the log Poisson model of anomalous scaling [21]. We find that the pdf has a number of strange and undesirable features. Chapter ?? presents an analytic example of a pdf that is self-similar yet satisfies the power law requirement with nonlinear exponents. This provides a specific example that anomalous scaling may be expressed through self-similarity; an idea that was believed to have sunk with K41. This is a specific example from the new theory proposed in [14]. Chapter ?? introduces the shell models which will be used to generate inertial range data for our analysis in subsequent chapters. Shell models are severe truncations of the Navier Stokes equations in Fourier space. We chose two specific models; GOY and Sabra, both are well known. Both shell models are crudely analogous to spectral Navier Stokes equations [5, 6]. In Chapter ??, we prove that the inviscid invariants, energy and helicity, are conserved for the truncated version of each model when the viscosity and forcing vanish. The truncated versions are what we actually solve numerically. Chapter ?? carries out the numerical simulations on each model and investigates how viscosity effects the results and the duration of a simulation. We also introduce structure functions, scaling laws, scaling exponents, and characteristic length scales. In Chapter ??, we look at the pdf for the time series of each shell variable. In particular, we show how the data in the inertial range can be collapsed using a similarity transformation. Furthermore, we inspect how well the power laws hold for each model. Chapter ?? reviews a new self-similarity theory built on the observed collapse of the data in Chapter ??. The functional equation for the pdf emerges from the theoretical analysis. Discarding the GOY model, Chapter 2, then applies the new theory to the data from the Sabra shell model. Chapter ?? wraps up the analysis of the theory and the shell model.

Chapter 2

APPLYING THE NEW SIMILARITY THEORY TO THE SHELL MODEL DATA

In the theoretical analysis in Chapter ??, we found the similarity formulas for the inertial range in terms of four constants β , n_0 , a , C_3 (five if ζ_3 is included) . While this may seem like many constants to determine, one should keep in mind that two constants are unavoidable. There has to be a characteristic length, ℓ_0 , equivalently, n_0 performs this function. Also, there has to be a constant characterizing the forcing rate, (related to the dissipation rate because this system is in equilibrium). C_3 performs this role. β and a came about through the functional equation (?? and ??). The theory does not provide values for these constants other than $0 < \beta < 3$ and $a < 0$.

In this chapter, we will use the data form the Sabra model to find β and a . Because the GOY model data does not meet our standards for the power law requirement, it cannot be expected to follow the theory. First, we show how the power laws can be plotted so as to reveal n_0 and C_3 . This is theoretically possible because we have found a universal expression for the coefficients C_p . The technique is to introduce rescaled structure functions. Second, we examine the data to see if the horizontal stretching fits the theoretical expression $(\ln \ell_0 - \ln \ell)^{1/\beta}$ or equivalently a power law in $n - n_0$. Likewise, we can check if the horizontal and vertical shifts are linear functions of n as predicted by the theory. Finally, we can extract β and a from the data.

2.1. Determination of n_0 and C_3 via Rescaled Structure Functions

When we previously defined structure functions, we neglected to include an intrinsic length scale. The intrinsic scale plays an important role in regard to the scaling coefficients, \tilde{C}_p . Without an intrinsic scale, the coefficients cannot be described in universal terms. The reason is that any factor of the form $2^{n_1\zeta_p}$ can be attached to the coefficient. In other words, we can write

$$\begin{aligned} S_p(n) &= \tilde{C}_p 2^{-n\zeta_p} \\ &= \tilde{C}_p 2^{n_1\zeta_p} 2^{-\zeta(n-n_1)} \end{aligned} \quad (2.1)$$

and redefine the coefficient as $\tilde{C}_p 2^{n_1\zeta_p}$. Only when we can fix n_1 at some preferred value, like an intrinsic scale n_0 , can we talk about universal coefficients. The theoretical formulas from the previous chapter [14] state

$$S_p(\ell) = C_p \left(\frac{\ell}{\ell_0} \right)^{\zeta_p}. \quad (2.2)$$

Using $\ell = 2\pi/k$, where $k = k_0 2^n$, we can translate to shell notation. Hence, we replace ℓ with $2\pi/(k_0 2^n)$, we get

$$\begin{aligned} S_p(n) &= C_p \left(\frac{2\pi/(k_0 2^n)}{2\pi/(k_0 2^{n_0})} \right)^{\zeta_p} \\ &= C_p \left(\frac{2^{n_0}}{2^n} \right)^{\zeta_p} \\ &= C_p 2^{-\zeta_p(n-n_0)}. \end{aligned} \quad (2.3)$$

To rescale the structure functions, we must know C_p . Again, we use the theoretical formula for the universal coefficients found in [14],

$$C_p = \frac{2}{p+2} \left(\frac{5C_3}{2} \right)^{p/3}. \quad (2.4)$$

Thus, (2.3) reads

$$S_p(n) = \frac{2}{p+2} \left(\frac{5C_3}{2} \right)^{p/3} 2^{-\zeta_p(n-n_0)}. \quad (2.5)$$

Next, we will take the natural logarithm of both sides:

$$\ln(S_p(n)) = \ln \left[\frac{2}{p+2} \left(\frac{5C_3}{2} \right)^{p/3} 2^{-\zeta_p(n-n_0)} \right] \quad (2.6)$$

or

$$\ln(S_p(n)) = \ln \left(\frac{2}{p+2} \right) + \frac{p}{3} \ln \left(\frac{5C_3}{2} \right) - \zeta_p(n-n_0) \ln 2 \quad (2.7)$$

then

$$\ln \left(\frac{S_p(n)(p+2)}{2} \right) = \frac{p}{3} \ln \left(\frac{5C_3}{2} \right) - \zeta_p(n-n_0) \ln 2. \quad (2.8)$$

Our final step is to move p to the left hand side

$$\frac{1}{p} \ln \left(\frac{S_p(n)(p+2)}{2} \right) = \frac{1}{3} \ln \left(\frac{5C_3}{2} \right) - \frac{1}{p} \zeta_p(n-n_0) \ln 2. \quad (2.9)$$

The left hand side is the data we plot. Whereas, the right hand side is the theoretical expression. When plotted against n , the theoretical expression calls for $1/p \ln \left(\frac{S_p(n)(p+2)}{2} \right)$ to form a set of straight lines (one for each p), with a single point in common, namely $(n_0, 1/3 \ln(5C_3/2))$.

It is for this reason we have introduced the rescaled structure functions. This is shown in Figure 2.1. Note, in the absence of anomalous scaling, i.e. $\zeta_p = p/3$, (2.9) produces the same straight line for all p . Thus, the spread of the lines in Figure 2.1 is a signature of anomalous scaling.

The theoretical expression is, of course, only valid when n is in the inertial range. By fitting straight lines to the power laws in the inertial range, as is done in Figure 2.1, we extrapolate to find the focusing point for all the lines. In fact, we observe that the lines have an approximate common point of intersection. The focusing confirms the theoretical expression for the scaling coefficients in (2.4). If (2.4) did not apply the lines would not intersect at the same point.

The common point of intersection forms the virtual origin for the inertial range. That is, the scaling laws cannot be continued to larger scales (smaller n). In fact, n_0 is the smallest n for $S_p(n)$ in (2.5) that corresponds to a pdf.

Figure 2.1 is significant for many reasons. Not only does it determine an intrinsic length scale for the inertial range, and confirm the theoretical coefficient formula (2.4), it also shows that all $S_p(n)$ can be computed from $S_p(\tilde{n})$ and the virtual origin, where \tilde{n} represents a single shell located inside the inertial range. This fact alone shows that the inertial range is self-similar. If we know all $S_p(\tilde{n})$ for some value of \tilde{n} , then the radial profile can be determined through an inverse Mellin transform. The similarity implied by Figure 2.1 then allows us to obtain the radial profile for all inertial range shells.

2.1.1. The Limit of $p \rightarrow 0$

Figure 2.2.a show where $p = 0$ would be in the graph of rescaled structure functions. This is due to (2.9) involving a division by zero for $p = 0$. Nonetheless, we can define a rescaled structure function for $p = 0$ through a limiting process. Figure 2.2.b clearly suggest that there are no problems for small p . On the right hand side of (2.9) it is the factor ζ_p/p that causes the problem. Since $\zeta_0 = 0$, L'Hopitals rule can be applied. In fact, the singularity at $p = 0$ is removable. We implement L'Hopitals rule for the data by means of a difference quotient:

$$\lim_{p \rightarrow 0} \tilde{S}_p = \lim_{p \rightarrow 0} \frac{\tilde{S}_p - \tilde{S}_{-p}}{2p}. \quad (2.10)$$

where

$$\tilde{S}_p = \frac{1}{p} \ln \left(\frac{S_p(n)(p+2)}{2} \right). \quad (2.11)$$

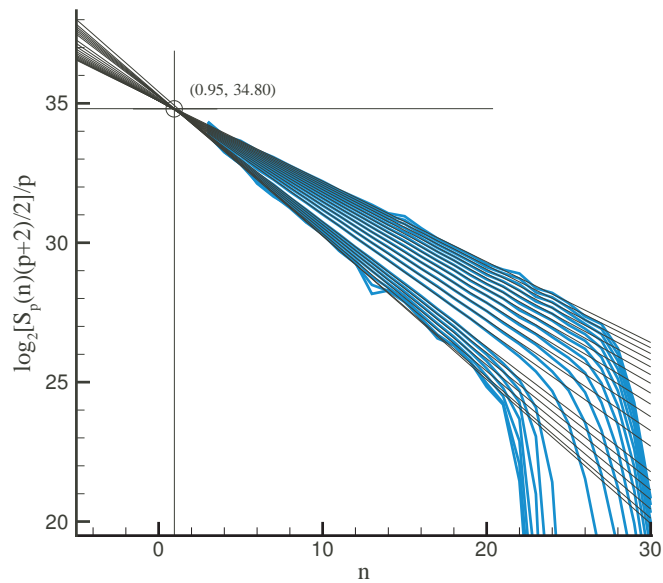


Figure 2.1. Rescaled structure function of Run 9 from Table A.2 (Sabra). The functions can be formed because we have found universal coefficients. $p = [-1.75, -1.5, \dots, -0.5, -0.25, 0, 0.5, 1.0, \dots, 11.5, 12.0]$

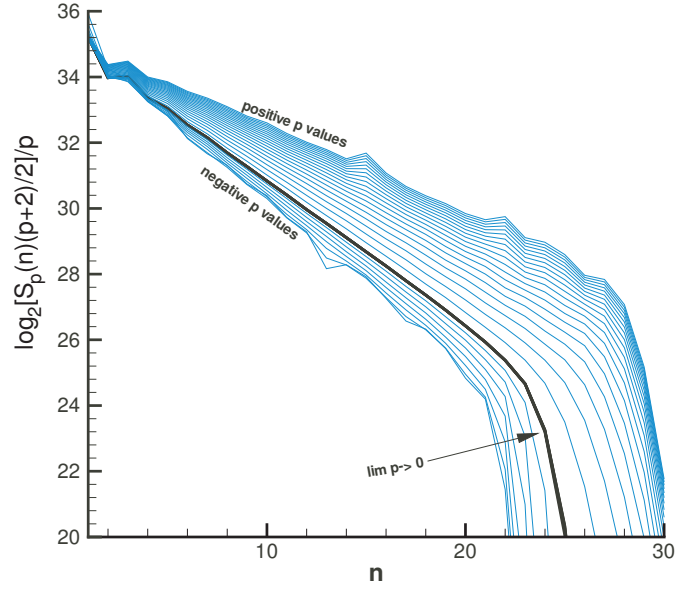
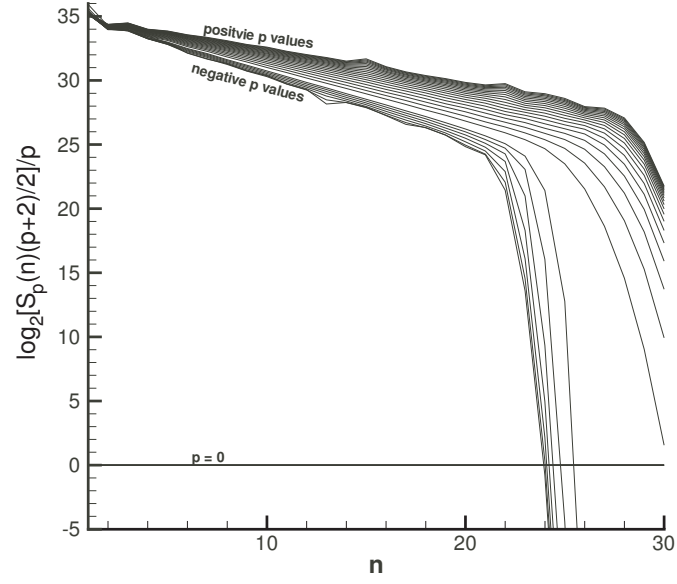


Figure 2.2. Rescaled structure function of Run 9 from Table A.2 (a) with $p = 0$ included. Note the gap between the negative and positive p values. (b) as $p \rightarrow 0$ where $0.1 \geq p \geq 0.01$. Clearly a limit exists.

2.2. Graphically Measured Collapse

Figure 2.3 show log-log plots of the radial profile $P_0(r; n)$ for n ranging from 3 to 20. As described in Chapter ??, these graphs can be made to collapse by a similarity transformation. Specifically, rigid horizontal shifts together with linear horizontal stretching. Both shifts and stretching can be measured. The process is as follows. We first select one reference shell in the middle of the inertial range. Let that be $n = 12$. The graphical objects corresponding to each of the other shells are then shifted rigidly and stretched horizontally so that the graphs match that of $P_0(r; 12)$ as shown in Figures ?? through ??. Because the axes from Figure 2.3 are attached to $P_0(r; n)$ we can readily identify the vertical shift. It is listed in Table 2.2. We can also identify matching abscissa on the fixed and transformed scale. The horizontal bars in Figure ?? through ?? are included for this purpose. The corresponding abscissa pairs are listed in Table 2.2. Since the transformation is linear only two values are needed for each n . From these values we calculate the horizontal stretching factor A and shift B , i.e.

$$x_{stretched} = Ax_f + B \quad (2.12)$$

Say a and b are two points on the fixed axis corresponding to c and d on the stretched axis, then

$$c = Aa + B \quad (2.13)$$

$$d = Ab + B. \quad (2.14)$$

So that,

$$A = \frac{a-b}{c-d} \tag{2.15}$$

$$B = \frac{bc-ad}{b-a}. \tag{2.16}$$

Figure ?? shows the vertical and horizontal shifts as functions of n . We observe that both are linear functions of n as called for by the theory. The scatter around the regression line is in part due to the matching of the graphical objects being done manually. The theory does provide analytical formulas to do a computational collapse. However, the data we obtained contained too much statistical noise. Therefore, we were not able to use the analytical formulas. The vertical shift is also shown. It forms a straight line on log-log scales. Consequently, the stretching is a power law in $(n - n_0)$ just as predicted by the theory. The slope is $1/\beta$ and we obtain $\beta = 1.23$ from the regression line.

Table 2.1. Measurements for scaling individual radial profiles. Shell 12 is selected as the radial profile to be scaled to. The fixed scale refers to the Shell 12 axis. The first pair of fixed and stretched scales refers to the initial alignment of the horizontal axis. The second pair refers to the terminal alignment of the horizontal axis.

<i>Measurements for Graphical Collapse</i>					
Shell	Fixed Scale	Stretched Scale	Fixed Scale	Stretched Scale	Vertical Shift
3	15	22.2	21.1	24	7
4	16.2	22	22.1	24	6.2
5	15.6	21	23.1	24	5.8
6	16	21	22.8	24	5.6
7	14.8	19	23.2	24	3.7
8	15.8	19	23.3	24	3.2
9	15.6	18	23.5	24	1.8
10	15.7	17	23.6	24	1.2
11	15.2	16	23.8	24	0.8
13	15.5	15	24.3	24	-0.7
14	17	15.7	24	23.6	-1.6
15	17	15.2	24	24.3	-2.4
16	18	15.6	24	23.3	-2.8
17	18	15.2	24	23.1	-3.9
18	19	16	24	22.8	-4.3
19	19	15.1	24	22.7	-5.8
20	20	16.1	24	22.6	-6.5

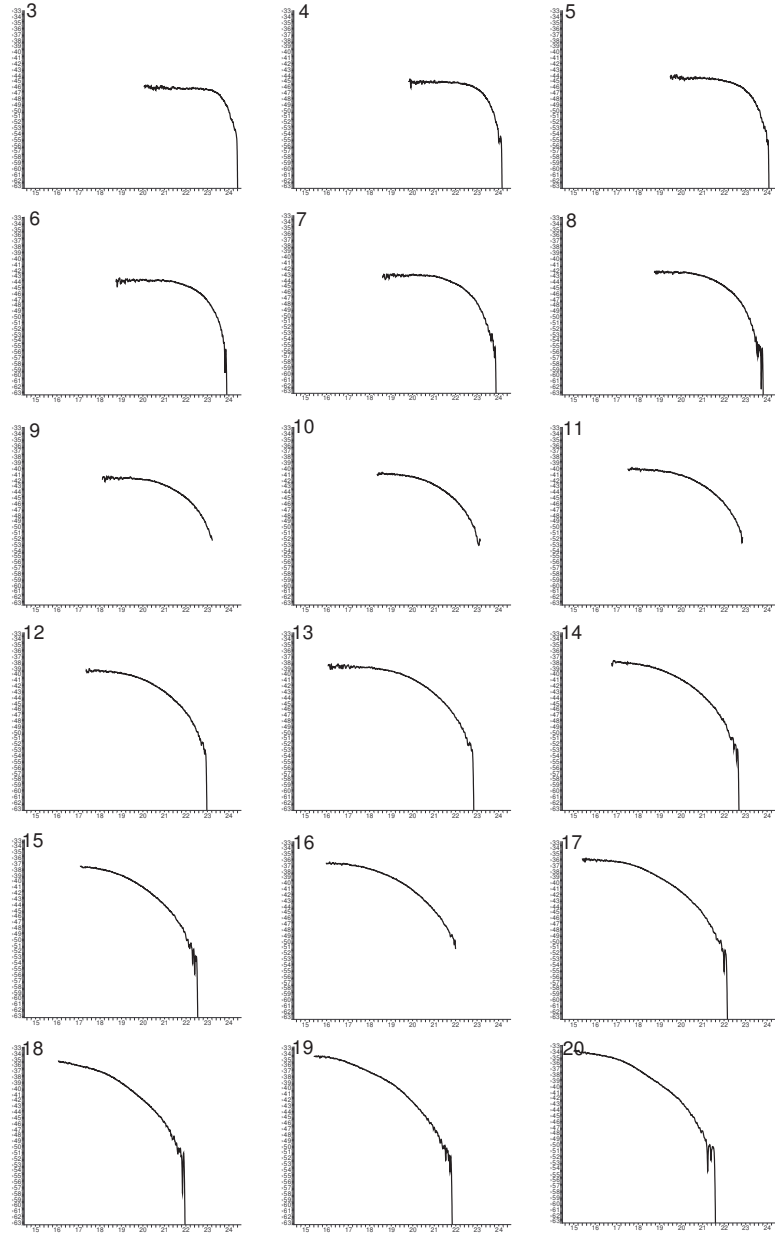


Figure 2.3. Individual plots of each of the radial profiles that have a similar curve. The radial profiles $P_0(r; n)$ plotted on log-log scales for $3 \leq n \leq 20$ for Sabra Run 9.

Appendix A

APPENDIX

A.1. Description of GOY Shell Model Runs and Table

In most cases, we have forced the models in the first shell so that the inertial range forms on the ultraviolet side. However, in run 2 from Table A.1, we force in shell seven and observe an infra-red inertial range form. Run 1 uses the parameters of [26] originally used. This run is used as a control and to reproduce Pisarenko et. al. [19] work. Run 2 is equivalent to Run 1 as far as the parameters are concerned. However, in this run, we force in shell 6. As a result, we see an infra-red inertial range. We can apply the affine collapse to this data as well. This result is of interest in the light of Carl Gibson idea that the true cascade in turbulence is from small to large scales [8]. We start with small forcing in Run 3. Here, the forcing is small enough that the solution is quasi-periodic and we have no inertial range. We can observe this in the distribution of u_n . In this particular case, the points were located in a ring that was centered at the origin (see Figure A.1). However, there is still circular symmetry about the origin in this case.

In order to obtain an inertial range which the new similarity theory requires, we increase the forcing for Run 4. In Run 4, we still have virtually no inertial range. We must increase the forcing further. In Run 5, the model is chaotic and we have somewhat more of an inertial range. Run 6 increases the forcing and the shell number, however we are not obtaining enough of an inertial range. In Run 7, we increase the forcing significantly. The number of shells remains the same, but this time, we observe a distinct inertial range. We want to observe how much forcing we can pump into the

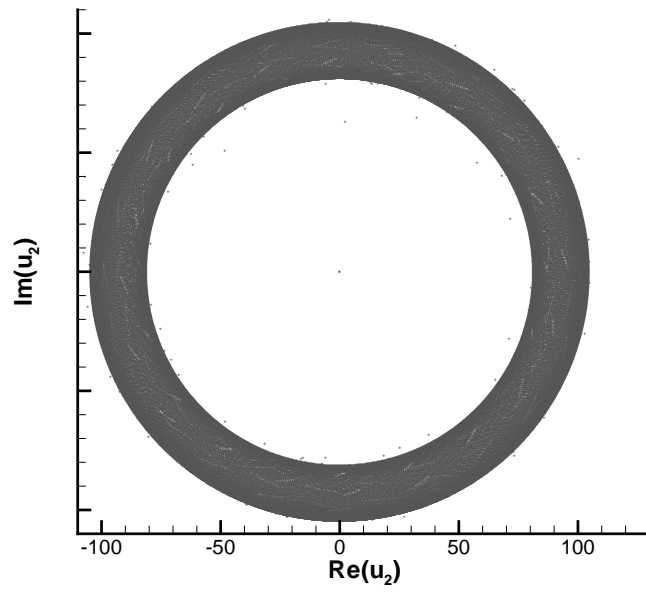


Figure A.1. Distribution of u_i . This plot displays the quasi-periodic nature of Run 3 for shell 10 (eps file).

system before numerical problems arise. Thus, we create Run 8 and Run 9. Run 10 is at the limit of what is numerically possible with out model. This run took four days to complete and is the longest run in the computation. However, this run is not long enough to generate a statically significant ensemble for the smaller shell numbers. Therefore, we have backed off in the forcing level and simulated a longer time series in Run 9.

Table A.1. Simulations with the GOY shell model with respective parameters. Run 1 uses the original GOY form found in (??). Runs 2-10 use the log polar form of GOY found in (??).

<i>Types of Runs Considered for Collapse</i>						
Run #	t_{end}	Forcing	ν	k_0	Forcing Shell	# Shells
1	2×10^4	$(1 + i) \times 5 \times 10^{-3}$	10^{-7}	2^{-4}	4	22
2	1×10^{-3}	$(1 + i) \times 2.048 \times 10^{16}$	1	1	7	26
3	1×10^3	$(1 + i) \times 10^5$	1	1	1	20
4	3×10^2	$(1 + i) \times 10^6$	1	1	1	20
5	5×10	$(1 + i) \times 10^7$	1	1	1	20
6	1×10	$(1 + i) \times 10^8$	1	1	1	23
7	1×10^{-3}	$(1 + i) \times 10^{12}$	1	1	1	23
8	1×10^{-6}	$(1 + i) \times 10^{16}$	1	1	1	27
9	1×10^{-8}	$(1 + i) \times 10^{20}$	1	1	1	30
10	1×10^{-10}	$(1 + i) \times 10^{23}$	1	1	1	36

A.2. Description of Sabra Shell Model Runs and Table

Like the GOY shell model, the Sabra shell models are forced in the first shell so that the inertial range forms on the ultraviolet side. However, in run 2 from Table A.2, forces in shell seven and we are able to observe an infra-red inertial range form. Run 1 uses the parameters of [26] originally used. This run is used to illustrate the

immediate differences between GOY and Sabra, i.e. oscillations in the inertial range. Figure ?? illustrates this. Run 2 is equivalent to Run 1 in log polar form. The parameters are equivalent to [26] in the original evaluation. However, in this run, we force in shell 7. As a result, we see an infra-red inertial range. The affine collapse can be applied to this data as well. The rest of the runs follow much the same as the GOY shell model. We again focus on Run 9 for the same reasons as GOY.

Table A.2. Simulations with the Sabra shell model with respective parameters. Run 1 uses the original Sabra form found in (??). Runs 2-10 use the log polar form of Sabra found in (??).

<i>Types of Runs Considered for Collapse</i>						
Run #	t_{end}	Forcing	ν	k_0	Forcing n	# of n
1	2×10^4	$(1+i) \times 5 \times 10^{-3}$	10^{-7}	2^{-4}	4	22
2	1×10^{-3}	$(1+i) \times 2.048 \times 10^{16}$	1	1	7	26
3	1×10^3	$(1+i) \times 10^5$	1	1	1	20
4	3×10^2	$(1+i) \times 10^6$	1	1	1	20
5	5×10	$(1+i) \times 10^7$	1	1	1	20
6	1×10	$(1+i) \times 10^8$	1	1	1	23
7	1×10^{-3}	$(1+i) \times 10^{12}$	1	1	1	23
8	1×10^{-6}	$(1+i) \times 10^{16}$	1	1	1	27
9	1×10^{-8}	$(1+i) \times 10^{20}$	1	1	1	30
10	1×10^{-10}	$(1+i) \times 10^{23}$	1	1	1	36

REFERENCES

- [1] *On the singularity structure of fully developed turbulence* (Amsterdam, 1983), North-Holland.
- [2] ANSELMET, F., GAGNE, Y., HOPFINGER, E. J., AND ANTONIA, R. A. High-order velocity structure functions in turbulent shear flows. *Journal of Fluid Mechanics* 140, -1 (1984), 63–89.
- [3] BATCHELOR, G. *The theory of homogeneous turbulence*. Cambridge University Press, Cambridge, 1971.
- [4] CHAMPAGNE, F. H. The fine-scale structure of the turbulent velocity field. *Journal of Fluid Mechanics* 86, 01 (1978), 67–108.
- [5] DITLEVSEN, P. Cascades of energy and helicity in the goy shell model of turbulence. *Phys. Fluids* 9, 5 (1997), 1482–1484.
- [6] DITLEVSEN, P., AND MOGENSEN, I. Cascades and statistical equilibrium in shell models of turbulence. *Phys. Rev. E* 53, 5 (1996), 4785–4793.
- [7] FRISCH, U. *Turbulence*. Cambridge University Press, Cambridge, 1999.
- [8] GIBSON, C. Turbulence in the ocean, atmosphere, galaxy, and universe. *Appl. Mech. Rev.* 49, 5 (1996), 299–315.
- [9] GRANT, H. L., STEWART, R. W., AND MOILLIET, A. Turbulence spectra from a tidal channel. *Journal of Fluid Mechanics Digital Archive* 12, 02 (1962), 241–268.
- [10] HINZE, J. *Turbulence; an introduction to its mechanism and theory*. McGraw-Hill, New York, 1959.
- [11] KOLMOGOROV, A. The local structure of turbulence in incompressible viscous fluid for very large reynolds numbers. *Reprinted Proc. R. Soc. Lond. (1991)* 434, 1890 (1941), 9–13.
- [12] LUNDGREN, T. Inertial range scaling law. *Journal of Turbulence* 6, 22 (2005).
- [13] MCCOMB, W. *The Physics of Fluid Turbulence*. Clarendon Press, Oxford, 1991.

- [14] MELANDER, M. V. Analysis of a symmetry leading to an inertial range similarity theory for isotropic turbulence, 2007. <http://www.citebase.org/abstract?id=oai:arXiv.org:physics/0702073>.
- [15] MELANDER, M. V., AND FABIJONAS, B. R. Self-similar enstrophy divergence in a shell model of isotropic turbulence. *J. Fluid Mech.* 463 (2002), 241–258.
- [16] MELANDER, M. V., AND FABIJONAS, B. R. Intermittency via self-similarity – an analytic example, 2005. <http://www.citebase.org/abstract?id=oai:arXiv.org:physics/0512198>.
- [17] MOSER, R. D., KIM, J., AND MANSOUR, N. N. Direct numerical simulation of turbulent channel flow up to $re_\tau = 590$. *Physics of Fluids* 11, 4 (1999), 943–945.
- [18] NOULLEZ, A., WALLACE, G., LEMPERT, W., MILES, R. B., AND FRISCH, U. Transverse velocity increments in turbulent flow using the relief technique. *Journal of Fluid Mechanics* 339, -1 (1997), 287–307.
- [19] PISARENKO, D., BIFERALE, L., COURVOISIER, D., FRISCH, U., AND VERGASSOLA, M. Further results on multifractality in shell models. *Phys. Fluids A* 5 (1993), 2533–2537.
- [20] ROSENBLATT, M., AND ATTA, C. V., Eds. *Statistical self-similarity and inertial subrange turbulence* (Berlin, 1993), vol. 12, Springer.
- [21] SHE, Z., AND LEVEQUE, E. Universal scaling laws in fully developed turbulence. *Phys. Rev. Lett.* 72, 3 (1994), 336–339.
- [22] SNEDDON, I. *Fourier Transforms*, 1st ed. McGraw Hill, New York, 1951.
- [23] TAYLOR, G. Statistical theory of turbulence. *Proc. Roy. Soc. A* 151 (1935), 421–478.
- [24] VINCENT, A., AND MENEGUZZI, M. The spatial structure and statistical properties of homogeneous turbulence. *Journal of Fluid Mechanics* 225, -1 (1991), 1–20.
- [25] YAKHOT, V., THANGAM, S., GATSKI, T., ORSZAG, S., AND SPEZIALE, C. Development of turbulence models for shear flows by a double expansion technique. Tech. Rep. 91-65, NASA ICASE, 1991.
- [26] YAMADA, M., AND OHKITANI, K. Lyapunov spectrum of a chaotic model of three-dimensional turbulence. *J. Phys. Soc. Jap.* 56, 12 (1987), 4210–4213.